INTERNATIONAL JOURNAL FOR NUMERICAL METHODS IN FLUIDS
Int. J. Numer. Meth. Fluids 2004; **44**:905–925 (DOI: 10.1002/fld.683)

Numerical analysis of the rotating viscous flow approaching a solid sphere

Yan-Xing Wang, Xi-Yun Lu*,† and Li-Xian Zhuang

Department of Modern Mechanics, University of Science and Technology of China, Hefei, Anhui 230026, People's Republic of China

SUMMARY

A numerical simulation is performed to investigate the flow induced by a sphere moving along the axis of a rotating cylindrical container filled with the viscous fluid. Three-dimensional incompressible Navier–Stokes equations are solved using a finite element method. The objective of this study is to examine the feature of waves generated by the Coriolis force at moderate Rossby numbers and that to what extent the Taylor–Proudman theorem is valid for the viscous rotating flow at small Rossby number and large Reynolds number. Calculations have been undertaken at the Rossby numbers (Ro) of 1 and 0.02 and the Reynolds numbers (Re) of 200 and 500. When $Ro = O(1)$, inertia waves are exhibited in the rotating flow past a sphere. The effects of the Reynolds number and the ratio of the radius of the sphere and that of the rotating cylinder on the flow structure are examined. When $Ro \ll 1$, as predicted by the Taylor–Proudman theorem for inviscid flow, the so-called 'Taylor column' is also generated in the viscous fluid flow after an evolutionary course of vortical flow structures. The initial evolution and final formation of the 'Taylor column' are exhibited. According to the present calculation, it has been verified that major theoretical statement about the rotating flow of the inviscid fluid may still approximately predict the rotating flow structure of the viscous fluid in a certain regime of the Reynolds number. Copyright © 2004 John Wiley & Sons, Ltd.

KEY WORDS: finite element method; rotating flow; vortex flow; wake

1. INTRODUCTION

Viscous flow past a sphere may be considered as a simple and typical case of the three-dimensional flow past bluff-bodies, which is significant in many engineering applications and in theoretical investigations [1]. The behaviour of the flow around a moving sphere

*Correspondence to: Xi-Yun Lu, Department of Modern Mechanics, University of Science and Technology of China, Hefei, Anhui 230026, People's Republic of China.
†E-mail: xlu@ustc.edu.cn

Contract/grant sponsor: National Science Fund for Distinguished Scholar; contract/grant number: 10125210
Contract/grant sponsor: Innovation Project of the Chinese Academy of Sciences; contract/grant number: KJCX-SW-L04
Contract/grant sponsor: Programme of Hundred-Talent of the Chinese Academy of Sciences

Received 25 June 2003
Revised 19 November 2003

at various Reynolds numbers has been investigated previously by researchers [2–9]. Taneda [2] performed experiments to visualize the wake downstream of a sting-mounted sphere for $5 < Re < 300$, where Re is the Reynolds number based on the sphere diameter D and the free stream velocity U. From the flow visualization, it was found that the flow separation from the rear part of the sphere surface appeared at $Re = 24$ approximately and formed an axisymmetric vortex ring thereby. Magarvey and Bishop [3] observed experimentally the wake of a free-falling drop of immiscible liquid through the water. The wakes of the liquid spheres exhibited a similar vortex ring structure to that reported by Taneda [2]. The vortex ring remained stable and axisymmetric up to $Re = 210$. In the range $210 < Re < 270$, the flow structure became non-axisymmetric and the vortex ring shifted off the plane perpendicular to the axis. By $Re = 270$, a double-thread wake was observed, which was unstable and eventually resulted in vortex shedding from the sphere, forming the so-called hairpin vortices. Those observations have also been demonstrated by Nakamura [5] for free-falling, fluid-filled spherical shells. The phenomenon of unsteady vortex shedding from a sphere has received great attention for $290 < Re < 400$. Some researchers [7–10] took measurements of the frequency about the unsteady wake and visualizations of the hairpin vortices shed from spheres. In the aspect of numerical computation, Tomboulides *et al.* [6, 11] performed a spectral element solution of viscous flow over a sphere for $25 < Re < 10^3$. They found that the initial separation appears at $Re = 20$, steady axisymmetric flow exists up to $Re = 212$, and a regular bifurcation, i.e. a transition from steady axisymmetric wake to the steady non-axisymmetric double-thread wake, occurs at $Re = 212$. Natarajan and Acrivos [12] studied the stability of the axisymmetric flow past a sphere using a finite element method and found the regular bifurcation at $Re = 210$. Shirayama [13] solved the flow past a sphere accelerating from rest up to $Re = 500$. Recently, Johnson and Patel [9] performed a numerical investigation of the flow past a sphere up to $Re = 300$ and claimed that steady axisymmetric flow should be observed at $Re < 200$; steady non-axisymmetric regime be presented at $210 < Re < 270$; and the unsteady flow with vortex shedding would appear at $Re = 270$ and higher.

Viscous flow over a rotating sphere has also received much attention in order to understand the effect of rotation on the flow. The characteristics of flow over the rotating sphere depend significantly on the direction of the rotation relative to the direction of the approaching flow. Two special directions of sphere rotating are usually taken to be representative ones, which are the streamwise rotation and the transverse rotation. Some work has been carried out to investigate the relation between the rotational speed and the force exerted on the sphere both for the cases of transverse rotation [14–18] and streamwise rotation [19–21] of the sphere. Schlichting [19] has summarized the previous results of flow over a streamwisely rotating sphere. The present authors have also performed a finite element analysis of the viscous flow past a sphere rotating in the streamwise direction [20]. To elucidate the character of this flow, the flow structures in the near wake at different Reynolds numbers and rotating speeds were examined. It was found that as the rotating speed of the sphere increased, the rotating effects got stronger and the vortex shedding under the effect of body rotation resulted in a swirling vortex structure in the near wake. Recently, another numerical simulation of viscous flow past a sphere rotating in the streamwise direction was conducted by Kim and Choi [21].

Flow induced by a sphere moving along the axis of a rotating fluid is a typical case of three-dimensional rotating flows past a rigid body of arbitrary shape. In this problem, the Rossby number is defined as $Ro = U/(\Omega D)$, where U is the moving velocity of the sphere along the axis of the rotating fluid, Ω represents the angular velocity of the rotating fluid, and

D is the diameter of the sphere. As indicated by Batchelor [22], 'determination of the flow due to a rigid body in steady translatory motion parallel to the axis of rotation is a difficult problem, and a clear picture of all aspects of the flow field is not yet available'. Taylor [23] firstly performed a famous experimental observation of the flow due to sphere moving in a rotating fluid at different Rossby numbers. Then, Long [24] carried out similar experimental visualization of the flow due to a moving body with spherical nose and conical tail in a rotating fluid and found that a column of fluid in front of the moving body was pushed ahead when the Rossby number is less than about 0.2–0.3. When the Rossby number is of order unity, the experimental observations showed, clearly, the existence of waves that were stationary relative to the body [24]. Yet, the flow structures in the wake of the moving body were ambiguous and unclear. Since then, the flow characters induced by a rigid body moving along the axis of a rotating fluid have been investigated theoretically and experimentally [25–33]. However, to the best of our knowledge, very little work was conducted numerically to depict the flow behaviour in detail.

The objective of this work is to reproduce numerically the inertia wave generated by the sphere moving in a rotating fluid at moderate Rossby numbers and to observe how the 'Taylor column' is evolved and eventually formed at a small Rossby number and large Reynolds number. A finite element method is employed to solve unsteady three-dimensional Navier–Stokes equations, which describe the evolution of the flow induced by a sphere moving along the axis of a rotating cylindrical container filled with the fluid. The Rossby number defined above is chosen to be of order $O(1)$, in one case, where the generation of inertial wave is examined for the viscous fluid flow at moderate-to-high Reynolds numbers. Another case is that $Ro \ll 1$, where the Taylor–Proudman theorem is re-examined for the viscous rotating flow. In particular, the evolution and formation of the 'Taylor column' are investigated.

This paper is organized as follows. Physical problem and mathematical formulation are given in Section 2. The numerical method and its validation are briefly described in Section 3. In Section 4, calculated results at $Ro \ll 1$ and of order unity are exhibited and discussed, respectively. Finally, concluding remarks are summarized in Section 5.

2. PHYSICAL PROBLEM AND MATHEMATICAL FORMULATION

As shown schematically in Figure 1, a cylindrical container without end-walls filled with the fluid rotates around its axis at a constant angular velocity $\mathbf{\Omega}$ in an inertial frame. In the cylinder, a rigid sphere moves at a constant velocity U along the axis of the cylinder and rotates about the axis of the cylinder at another constant angular velocity $\mathbf{\Omega}_S$ parallel to $\mathbf{\Omega}$. Then, the flows past the sphere at various Re and Ro numbers are numerically investigated.

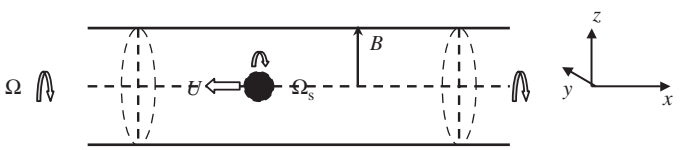

Figure 1. Sketch of a moving sphere in a rotating cylindrical container without end-walls filled by fluids.

The rotating cylinder surface is the outer boundary of the fluid flow, which simulates the experimental visualizations [23, 24]. On the other hand, the sphere may be influenced by the viscous fluid flow and rotates around the axis of the cylinder. The magnitude of rotating angular velocity of a free sphere depends on some flow and geometry parameters, which should be between zero and $|\boldsymbol{\Omega}|$, i.e. $0 \leqslant |\boldsymbol{\Omega}_S| \leqslant |\boldsymbol{\Omega}|$. An accurate value of the rotation velocity of the sphere can only be obtained by solving coupled equations of the fluid flow and the sphere motion simultaneously. In this study, however, our attention is paid to the flow structure rather than the coupling effect of the fluid flow and the sphere motion. So, we simply assume that the sphere rotates around the axis of the cylinder at some prescribed angular velocities $|\boldsymbol{\Omega}_S|$.

In the present calculation, a reference frame, which moves with the sphere and rotates with the rotating cylindrical container as a whole, is employed. Three-dimensional Navier–Stokes equations for the incompressible fluid of uniform density are non-dimensionalized by the diameter D and the moving velocity U of the sphere as the length and velocity scales, respectively. Then, the non-dimensional equations are written as

$$\frac{\partial \boldsymbol{u}}{\partial t} + \boldsymbol{u} \cdot \nabla \boldsymbol{u} + \frac{2}{Ro}\, \boldsymbol{e}_x \times \boldsymbol{u} = -\nabla p + \frac{1}{Re}\, \nabla^2 \boldsymbol{u} \tag{1}$$

$$\nabla \cdot \boldsymbol{u} = 0 \tag{2}$$

where $\boldsymbol{e}_x = \boldsymbol{\Omega}/|\boldsymbol{\Omega}|$ represents the unit vector in the axial direction, Re is the Reynolds number defined as $Re = UD/\nu$ and Ro is the Rossby number defined as $Ro = U/(|\boldsymbol{\Omega}|D)$ with ν representing the kinematic viscosity. The centrifugal force is incorporated into the pressure term.

The initial conditions used in the present calculation are $\boldsymbol{u} = \boldsymbol{e}_x$, $p = 0$ at $t = 0$. The boundary conditions are as follows: $\boldsymbol{u} = \boldsymbol{e}_x$, $\partial p/\partial x = 0$ on the inlet boundary of the cylindrical container ($x \to -\infty$); $\partial \boldsymbol{u}/\partial x = 0$ and $p = 0$ for the downstream condition ($x \to \infty$); $\boldsymbol{u} = \boldsymbol{e}_x$ and $\partial p/\partial r = (1/Re)\partial^2 u_r/\partial r^2$ on the cylinder's wall, i.e. $r = (y^2 + z^2)^{1/2} = B$ and $-\infty < x < \infty$, where u_r represents the radial velocity component; and $\boldsymbol{u} = -(\boldsymbol{\Omega} - \boldsymbol{\Omega}_S) \times \boldsymbol{r}$ on the sphere surface, i.e., $|\boldsymbol{r}| = \frac{1}{2}$, where B is constant and represents the radius of the cylinder, as shown in Figure 1.

3. NUMERICAL METHODS

In this calculation, a finite element method is employed to solve Equations (1) and (2). The velocity correction method is used to perform the time integration. Spatial discretization is carried out by the Galerkin weighted residual method. Upon the velocity correction method proposed by Kovacs and Kawahara [34], the computational loop in the present calculation is briefly described as follows:

Step 1: Calculation of the 'intermediate-velocity' field by applying the explicit first-order Euler scheme to Equation (1) at the first step,

$$\hat{\boldsymbol{u}} = \boldsymbol{u}^n - \Delta t \left[-\frac{1}{Re} \nabla^2 \boldsymbol{u}^n + (\boldsymbol{u}^n \cdot \nabla)\boldsymbol{u}^n + \frac{2}{Ro}\, \boldsymbol{e}_x \times \boldsymbol{u}^n \right] = \boldsymbol{u}^n - \Delta t \boldsymbol{F}(\boldsymbol{u}^n) \tag{3a}$$

Then, a second-order Adams–Bashforth scheme is employed in the following time step:

$$\hat{\boldsymbol{u}} = \boldsymbol{u}^n - \tfrac{1}{2}\Delta t[3\boldsymbol{F}(\boldsymbol{u}^n) - \boldsymbol{F}(\boldsymbol{u}^{n-1})] \tag{3b}$$

Step 2: Solution to the pressure Poisson equation obtained by setting $\boldsymbol{u}^{n+1} = \hat{\boldsymbol{u}} - \Delta t \cdot \nabla p^{n+1}$, then performing a divergence operation on it and forcing $\boldsymbol{u}^{n+1}$ to satisfy the incompressible constraint,

$$\nabla^2 p^{n+1} = \frac{1}{\Delta t}\nabla \cdot \hat{\boldsymbol{u}} \tag{4}$$

Step 3: Correction of the 'intermediate-velocity' field by adding the pressure term neglected in Equation (3) to the 'intermediate-velocity' field,

$$\boldsymbol{u}^{n+1} = \hat{\boldsymbol{u}} - \Delta t \nabla p^{n+1} \tag{5}$$

where the superscript n indicates the number of the time step, and Δt is the time step increment.

The finite element discretization of Equations (3)–(5) is taken by using the Galerkin weighted residual method via the following expansions in the piecewise polynomial basis functions:

$$\boldsymbol{u}(x, y, z, t) = \sum_{i=1}^{N} \boldsymbol{u}_i(t)\varphi_i(x, y, z) \tag{6a}$$

$$p(x, y, z, t) = \sum_{i=1}^{N} p_i(t)\varphi_i(x, y, z) \tag{6b}$$

where N represents the node number for the velocity and pressure. The weak solution form of (3)–(5) permits φ_i to be discontinuous in the first-order derivatives and subjected to the natural boundary conditions. Thus $\varphi_i(x, y, z)$ is chosen to be a C^0 piecewise bilinear basis function defined on iso-parametric rectangular elements. Substituting Equation (6) into the weak solution form of Equations (3)–(5), we can reach the discretized system of algebraic equations to be numerically solved. The details of relevant discretized formulation for the solution of the time-dependent incompressible Navier–Stokes equations were described by Kovacs and Kawahara [34]. In our previous study, some validations by using the finite element approach have already been carried out [20, 35].

To further validate and verify the computational method and code to be used, two problems are considered here. One is the viscous flow around a stationary sphere, and another the viscous flow past a sphere rotating in the streamwise direction. According to calculated results for the viscous flow over a stationary sphere, Table I lists the drag coefficient of the present calculation together with previous data [9, 21, 36, 37], where the time-averaged values of the drag coefficient are obtained only for $Re = 300$ (i.e. unsteady flow) and other values correspond to the asymptotic constant values of the drag coefficient for $Re = 100$ and 250 (i.e. steady flow). It is found that the present results agree very well with the previous data. As the typical criteria, the separation angle θ_s that is measured from the front stagnation point of the sphere and the separation bubble length x_s that is taken from the centre of the sphere to the point where the axis is crossed by the bubble are shown in Figure 2. It can be seen that the present calculated results are also in good agreement with the previous computational and experimental

Table I. Drag coefficient for viscous flow over a stationary sphere.

	Present			Fornberg [37]	Johnson and Patel [9]		Constantinescu and Squires [36]		Kim and Choi [21]		
Re	100	250	300	100	250	300	250	300	100	250	300
$\bar{C}_D$	1.086	0.701	0.656	1.085	0.70	0.656	0.70	0.655	1.087	0.702	0.657

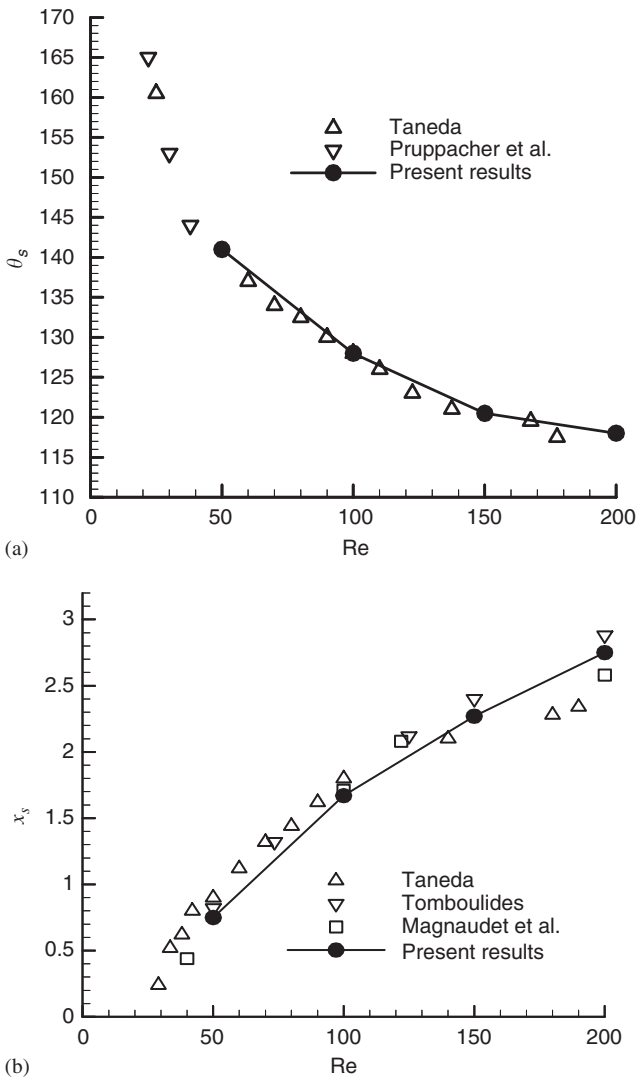

Figure 2. Flow geometry versus Reynolds number: (a) Polar separation angle θ_s. (b) Separation bubble length x_s.

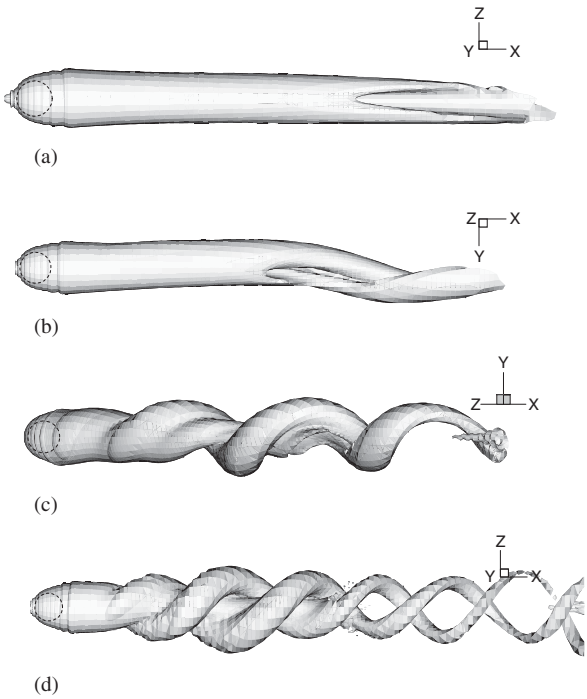

Figure 3. Iso-surface of vorticity magnitude ($|\omega| = 0.2$) for viscous flow past a sphere rotating in the streamwise direction at $Re = 250$: (a) $|\mathbf{\Omega}_S| = 0.1$; (b) $|\mathbf{\Omega}_S| = 0.5$; (c) $|\mathbf{\Omega}_S| = 1$; (d) $|\mathbf{\Omega}_S| = 2$.

data [2, 6, 38, 39]. Furthermore, we have found that steady axisymmetric flow is observed at $Re < 200$, steady non-axisymmetric flow and unsteady flow with vortex shedding are predicted at $210 < Re < 270$ and $270 < Re < 300$, respectively, which confirm that the present calculations agree well with the previous numerical results [6, 38, 39] and experimental measurements [2].

Validations were also performed for the viscous flow past a sphere rotating in the streamwise direction. Figure 3 shows the vortical structure with different rotating speeds at $Re = 250$. The streamwise vorticity in the wake was strengthened with the increase of the rotating speed of the sphere (i.e. $|\mathbf{\Omega}_S|$). If the rotating speed increases further as shown in Figure 3(d), the vortical structure is twisted into a complex pattern. Those vortical structures in the wake shown in Figure 3 are in good agreement with the patterns predicted by Kim and Choi [21]. To elucidate the detailed characters of this flow in the near wake, the flow structures at different Reynolds numbers and rotating speeds were shown in our previous paper [20].

In this study, to investigate the flow induced by a sphere moving along the axis of a rotating cylindrical container filled with the fluids (Figure 1), the size of computational domain in the axial direction is $20D$ ahead and behind the sphere, which is verified to be big enough according to the computational test. The time step is 0.001. The grid size is 150×120 in the axial and azimuthal directions, respectively. In the radial direction, the grid size is 60 for $B = 5$ and 7.5, and 120 for $B = 11$, 12.5, and 15. To increase the grid resolution near the solid boundaries, stretching transformations are employed. The grid size and time step independence of the present calculation has been ensured for every simulation and is exhibited in the following section for some typical case. Based on our validation and verification, it

can be confirmed that our calculation is reliable for the prediction of the flow induced by a sphere moving along the axis in a rotating fluid.

4. RESULTS AND DISCUSSION

4.1. Preliminary remarks

When the flow is induced in a fluid rotating as a whole, the fictitious Coriolis force acts as an elastic force and provides a restoring mechanism, which enables the waves to occur in the rotating fluid and propagate along the direction of the rotation axis. These waves are sometimes referred to as inertia waves (or Rossby waves). Usually, the ratio of the magnitude of the inertia and Coriolis forces, known as the Rossby number, is taken to be a convenient measurement of the importance of the Coriolis force.

A simple and typical case for the rotating fluid flow is the rotating pipe flow in a straight circular tube with contractive cross-sections. An elegant mathematical expression has been found for the description of a wave-like inviscid flow possibly occurring far downstream to the contraction of this tube at some suitable range of Rossby number, which is (Batchelor [22])

$$\psi = ArJ_1\{(k^2 - \alpha^2)^{1/2}r\}\sin\{\alpha(x + Ut)\} \tag{7}$$

where ψ is the Stokes stream function, $k = 2\Omega/U$, $\alpha = 2\pi/\lambda$ is the wavelength, $J_1(x)$ denotes the first-order Bessel function of the first kind. The frame of reference used is fixed to the rigidly rotating fluid far upstream, so there is a travelling-wave propagating relative to the approaching fluid at the speed U. Using the boundary condition $\psi = 0$ on the wall of downstream tube, one obtains,

$$J_1\{(k^2 - \alpha^2)^{1/2}B\} = 0 \tag{8a}$$

or

$$B(k^2 - \alpha^2)^{1/2} = Ro_{\mathrm{p}}^{-1}(1 - \Lambda^{-2})^{1/2} = x_n \tag{8b}$$

where x_n is the nth zero of the Bessel function $J_1(x)$, n denotes the number of wave train, $Ro_{\mathrm{P}} = U/(2\Omega B)$, and $\Lambda = k/\alpha$ is the non-dimensional wave length and usually is determined by Ro and x_n.

In the present study, a rotating viscous flow in a cylindrical container is induced by a sphere moving upstream at a constant velocity U. The example analysed above may throw some light on the understanding of the present numerical results at moderate Rossby numbers, which do exhibit obviously the wave pattern in the rotating flow past a sphere. When $Re \gg 1$, the fluid flow behaves like an inviscid flow except in the boundary layer and the wake of the sphere. This explains that, if Ro is in a proper range, in particular, not too large, the inertia wave may appear in the rotating flow past a rigid body. According to the above analysis, the condition for the inertia wave to appear in our case can be supposed as

$$\frac{2\Omega B}{U} = \frac{\Omega D}{U}\frac{2B}{D} > \frac{2B}{D}Ro_{\mathrm{c}}^{-1} \tag{9a}$$

i.e.

$$Ro = U/(\Omega D) < Ro_{\mathrm{c}} \tag{9b}$$

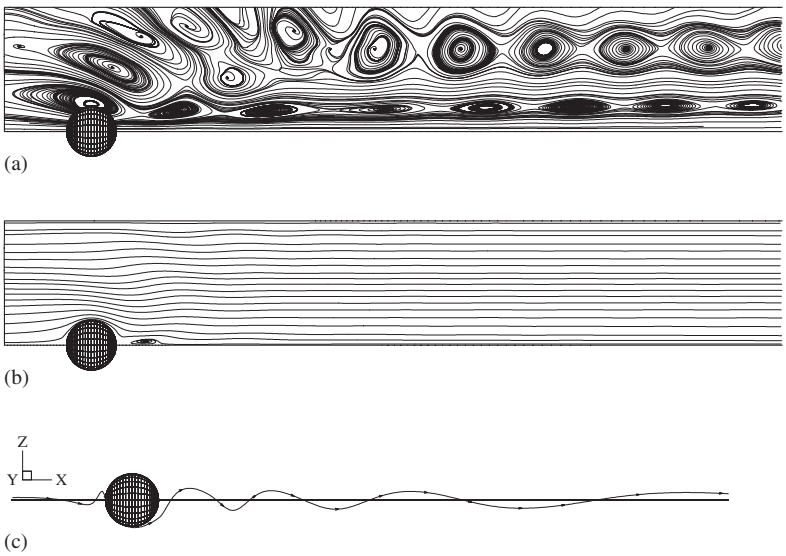

Figure 4. Instantaneous streamlines at $Ro = 1$, $Re = 200$, $B = 5$ and $|\mathbf{\Omega}_S| = |\mathbf{\Omega}|$: (a) in the reference frame $\mathbf{S}_1$; (b) in the reference frame $\mathbf{S}_2$; (c) three-dimensional swirling streamline in the reference frame $\mathbf{S}_2$.

where Ro_c is some critical Rossby number that is similar to the critical value of Ro_P in the convergent pipe flow discussed above. Based on this argument, it is expected that if the rotating angular velocity Ω of the far upstream flow is large enough, the inertia wave may indeed be generated. In the present study, we tentatively choose the Rossby number $Ro = 1$ to examine if the wave motion can occur in the rotating flow past a sphere, and then the effect of the ratio between the radii of the cylinder and of the sphere on the wave patterns is investigated.

4.2. Flow structures at moderate Rossby number

For completeness, our calculations for validation shown in Section 3 on the non-rotating flow past a solid sphere will be taken as the case of rotating flow at extremely large Rossby numbers and not repeatedly discussed here. In the present study, we mainly investigate the flow structure at moderate Rossby numbers of $Ro \sim O(1)$ and small Rossby numbers of $Ro \ll 1$, and the Reynolds numbers are taken to be 200 and 500. To demonstrate the effect of the radius of the cylindrical container on flow patterns, a series of radii of the rotating cylinder are chosen to be $B = 5$, 7.5, 11, 12.5, and 15. Here, we will not deal with the coupled problem of the viscous flow and the rotating sphere motion but simply prescribe the rotating angular velocity of the sphere separately to be $|\mathbf{\Omega}_S| = |\mathbf{\Omega}|$, $|\mathbf{\Omega}|/2$ and 0, instead. The effect of the angular velocity of the rotating sphere on the flow structure will be examined later in Section 4.4.

Instantaneous streamlines at $Ro = 1$, $Re = 200$, $B = 5$, and $|\mathbf{\Omega}_S| = |\mathbf{\Omega}|$ are shown in Figure 4. According to our calculated results, the flow is axisymmetric and then the flow pattern in a meridian plane (i.e. $\theta = 0°$) is illustrated. Figure 4(a) shows the streamlines in a reference frame (denoted by $\mathbf{S}_1$) fixed to the rotating cylinder, in which the sphere is moving through

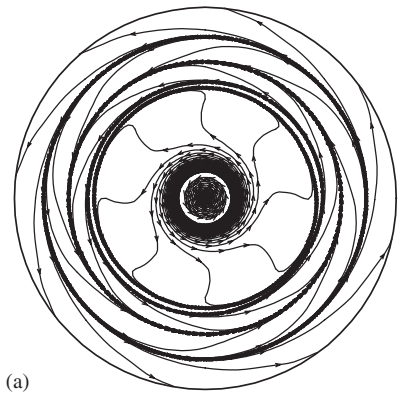

(a)

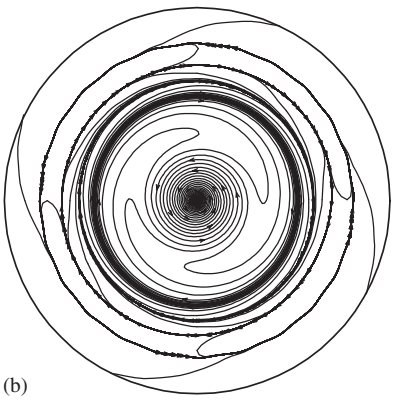

(b)

Figure 5. Instantaneous streamlines in the transverse plane at $Ro = 1$, $Re = 200$, $B = 5$ and $|\mathbf{\Omega}_S| = |\mathbf{\Omega}|$: (a) $x = 25$; (b) $x = 30$.

the fluid at a constant velocity U along the axis of the cylinder (as shown in Figure 1). It is seen that there are two rows of inertia wave cells, moving together with the sphere toward the left direction along the axis of the cylinder. The streamlines of the same flow observed in another reference frame (denoted by $\mathbf{S}_2$) fixed to the rotating sphere, are shown in Figure 4(b) and a steady wavy flow pattern is exhibited. The steadiness of the flow in $\mathbf{S}_2$ indicates that the wave propagates at a constant speed U relative to the ambient fluids. As the velocity of the incoming flow in $\mathbf{S}_2$ is much larger than the transverse oscillating speed of the fluid particle, the amplitude of wavy streamlines is very small, so that the wave looks quite different from that shown in Figure 4(a), where the axial velocity of fluid particles is as small as the transverse velocity and results in the well-organized cell patterns. It is noted that the azimuthal velocity of the flow is not zero although the inertia waves exhibit axisymmetric behaviour. The three-dimensional swirling streamline in the reference frame $\mathbf{S}_2$ is shown in Figure 4(c). To demonstrate the streamlines in the transverse plane, Figure 5 shows the streamline patterns at $x = 25$ and 30. As the azimuthal velocity is not zero, a swirl structure appears in the wake. In the central region of the wake, the azimuthal velocity is high and a strong vortex roll induced by stretching the streamwise vortex tube occurs. In the outer region of the wake,

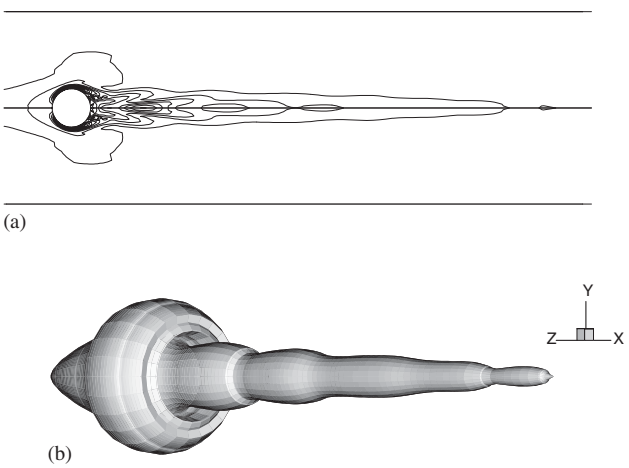

Figure 6. Vorticity magnitude contours at $Ro = 1$, $Re = 200$, $B = 5$ and $|\mathbf{\Omega}_S| = |\mathbf{\Omega}|$: (a) Contours in meridian plane. (b) Three-dimensional reconstruction of the vorticity iso-surface.

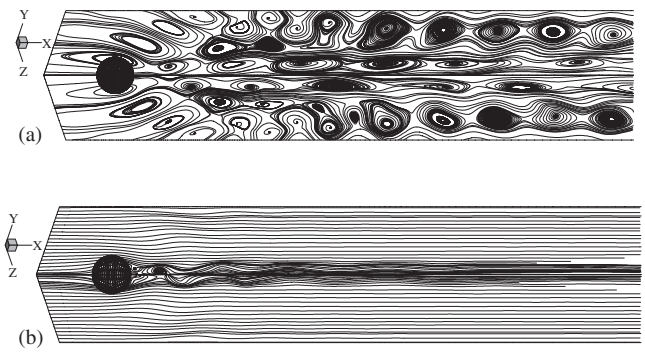

Figure 7. Instantaneous streamlines at $Ro = 1$, $Re = 500$, $B = 5$ and $|\mathbf{\Omega}_S| = |\mathbf{\Omega}|$: (a) in the reference frame $\mathbf{S}_1$ in two meridian planes perpendicular to each other; (b) in the reference frame $\mathbf{S}_2$.

however, the azimuthal velocity is rather small and the flow is only slightly swirled. Figure 6 shows contours of the azimuthal component of vorticity in meridian plane (Figure 6(a)) and a three-dimensional reconstruction of the vorticity iso-surface (Figure 6(b)).

To illustrate the effect of Reynolds number on the flow field, Figure 7 shows streamlines in two meridian planes (i.e. $\theta = 0°$, $\pi/2$) at $Ro = 1$, $Re = 500$, $B = 5$, and $|\mathbf{\Omega}_S| = |\mathbf{\Omega}|$. The streamline pattern in the reference frame $\mathbf{S}_1$ also exhibits two columns of wave cells. This indicates that the number of the radial cell is independent of the Reynolds number. However, flow structures at $Re = 200$ and 500 are obviously different. In the case of $Re = 500$, these wave cells are set in a staggered arrangement, and the flow field is no longer axisymmetric. This is because the periodic vortex shedding from the sphere results in a swirling vortex structure in the near wake of the sphere at this Reynolds number. The corresponding streamlines observed in the reference frame $\mathbf{S}_2$ are shown in Figure 7(b). The azimuthal vorticity contours in the longitudinal plane are shown in Figure 8 at four different phases in one cycle, and the unsteady

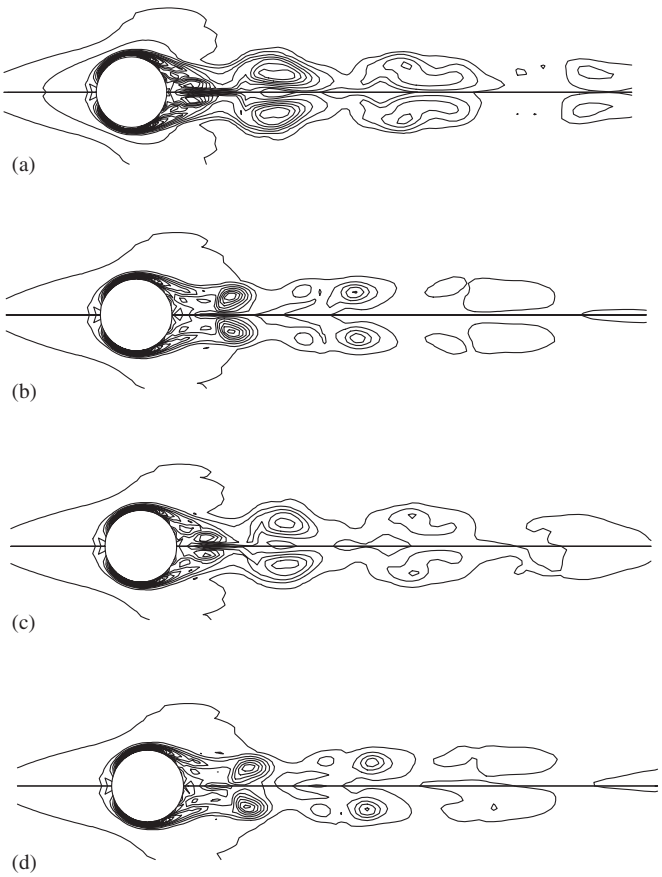

Figure 8. Vorticity contours in the longitudinal plane at four phases in one period for $Ro = 1$, $Re = 500$, $B = 5$ and $|\mathbf{\Omega}_S| = |\mathbf{\Omega}|$: (a) 0; (b) $T/4$; (c) $T/2$; (d) $3T/4$.

vortex shedding is clearly illustrated. To depict the swirling vortex shedding structures in the wake of the sphere, the corresponding patterns of three-dimensional vorticity iso-surface are shown in Figure 9. The swirling vortex structure is shed from the sphere to the wake at larger Reynolds number and changes the wave cells in the outer region of the wake to a staggered arrangement. Furthermore, Figure 10 shows the variation of the radial velocity with time at two different radial locations in the core and outer regions of the wake. In the outer wake of the sphere (at $r = 3.22$), the radial velocity component has small oscillatory amplitude due to the slight influence of the vortex shedding on the inertia wave. However, in the core region of the wake (at $r = 0.87$), the radial velocity component exhibits much larger amplitude because of the vortex shedding. To verify that the computed results in the present calculation are independent of the time step and the grid size, the results calculated by two different grid sizes and time steps have been shown in Figure 10.

It should be indicated that an upper critical Rossby number has been defined in Equation (9). For $Ro > Ro_c$, the Coriolis force is too small to form the inertia wave. Meanwhile, there

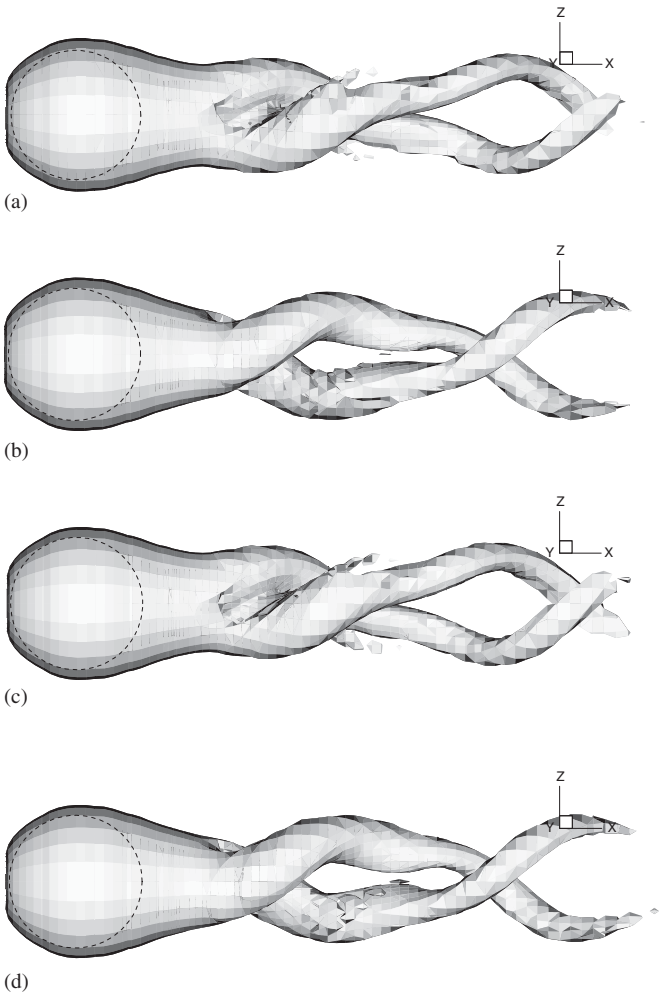

Figure 9. Vorticity iso-surface at four phases in one period for $Ro = 1$, $Re = 500$, $B = 5$, and $|\mathbf{\Omega}_S| = |\mathbf{\Omega}|$: (a) 0; (b) $T/4$; (c) $T/2$; (d) $3T/4$.

is also a lower critical Rossby number for the existence of the inertia wave. When the Rossby number gets smaller and smaller, the rotating inertia gets stronger and stronger and makes the streamlines to be stiffer and stiffer. In this circumstance, it is also impossible for the inertia wave to be generated. Actually, we have calculated the flow at a smaller Rossby number of $Ro = 0.5$ (not shown here because of the scope limitation) and have not found the formation of the inertia wave.

4.3. Effect of the radius of the cylinder on flow field

The wavelength of the inertia wave $\lambda = 2\pi/\alpha$ depends on several parameters, such as Ω, U, B and D. For a rotating fluid motion in a convergent tube, λ (or α) depends on Ω, U and

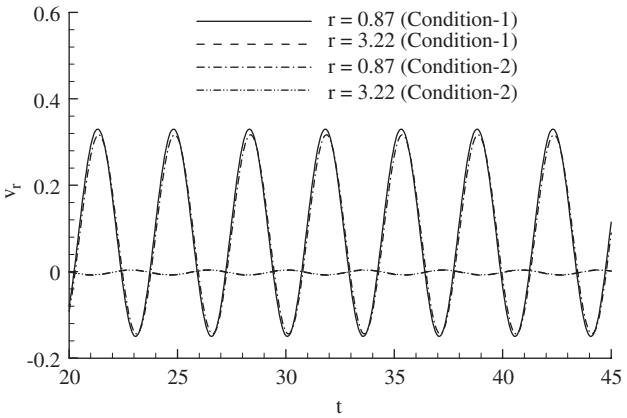

Figure 10. Variation of the radial velocity with time at two radial locations for $Ro = 1$, $Re = 500$, $B = 5$ and $|\mathbf{\Omega}_S| = |\mathbf{\Omega}|$: Condition—1: grid size $150 \times 120 \times 60$ and time step 0.001; Condition—2: grid size $300 \times 240 \times 120$ and time step 0.0005.

B, cf. Equation 8(b). Although the relation given by Equation 8(b) is not exactly applicable to the present problem, it will certainly be helpful to the understanding of the flow described here.

Now, N $(N = 1, 2, \ldots)$ denotes the column number of the wave cells. We can write an expression similar to (8b) in the form of

$$\left\{ Ro^{-2} - \left(\frac{\pi D}{\lambda} \right)^2 \right\} \left(\frac{2B}{D} \right)^2 = x_N \left(\frac{D}{B} \right) \tag{10}$$

when Ro and (D/B) are given, x_N, $N = 1, 2, \ldots$, can be regarded as some eigenvalues in the present problem. The number of wave train N and the wave length (λ/D) are then determined by Ro and (B/D).

According to the above analysis, the flow patterns will change with the cylinder radius at moderate Rossby numbers. To illustrate the effect of the cylinder radius on the flow field, Figure 11 shows streamlines plotted in the reference frame $\mathbf{S}_1$ in two mutually perpendicular meridian planes (i.e. $\theta = 0°$, $\pi/2$) at $B = 7.5$, 11, 12.5, and 15, $Ro = 1$, $Re = 500$ and $|\mathbf{\Omega}_S| = |\mathbf{\Omega}|$. The flow structure at $B = 5$, as shown in Figure 6(a), exhibits two columns of wave cells. At $B = 7.5$, three columns of wave cells are exhibited. The inner column of cells in the near wake evolves with time because of the influence of the vortex shedding on the near wake of the sphere. However, the outer two-column cells have almost steady wave character in the reference frame $\mathbf{S}_2$. If the radius of the cylinder increases further, e.g. $B = 11$, 12.5, and 15, as shown in Figure 11, the column number of the inertia wave cells may increase with the increase of the cylinder radius. Like the case of $B = 7.5$, the inertia wave cells of outer columns at larger B behave as steady waves in $\mathbf{S}_2$ while unsteadiness appears in the inner column near the wake of the sphere.

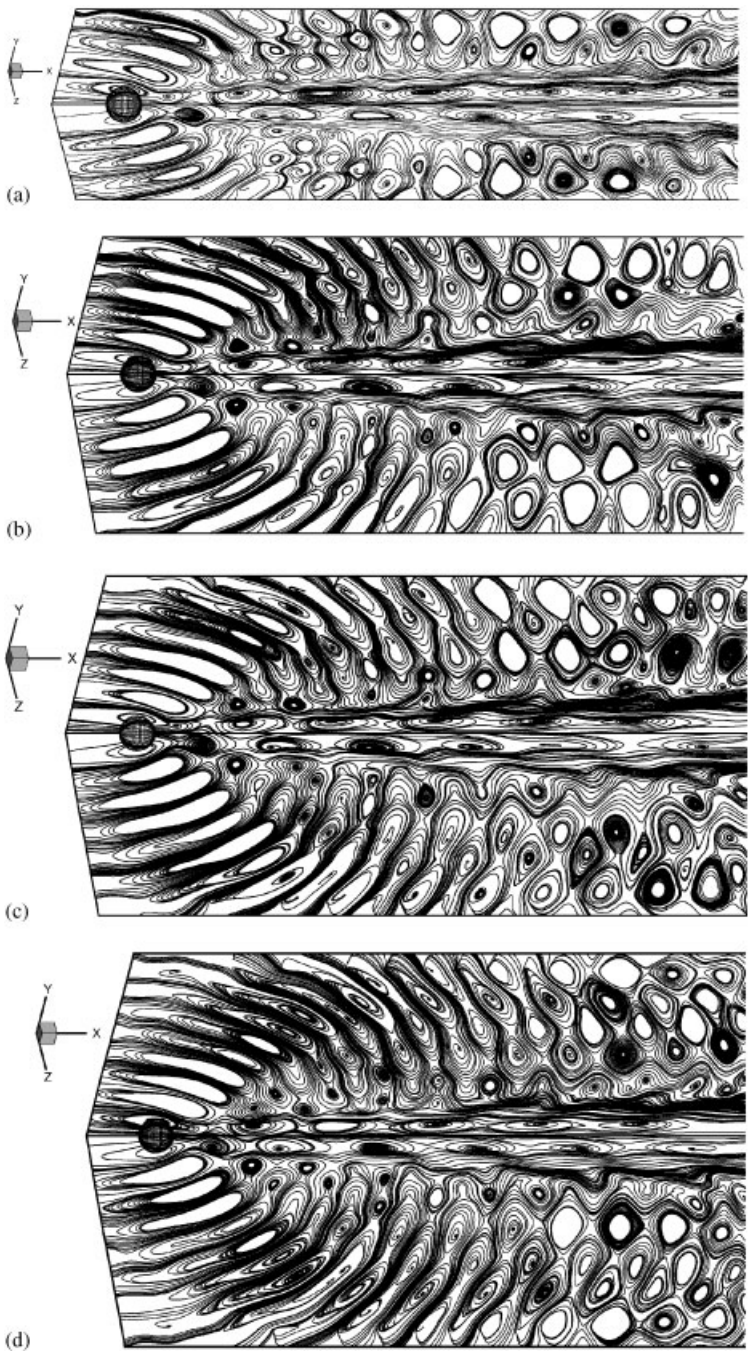

Figure 11. Instantaneous streamlines in the reference frame $\mathbf{S}_2$ at $Ro = 1$, $Re = 500$ and $|\boldsymbol{\Omega}_S| = |\boldsymbol{\Omega}|$: (a) $B = 7.5$; (b) $B = 11$; (c) $B = 12.5$; (d) $B = 15$.

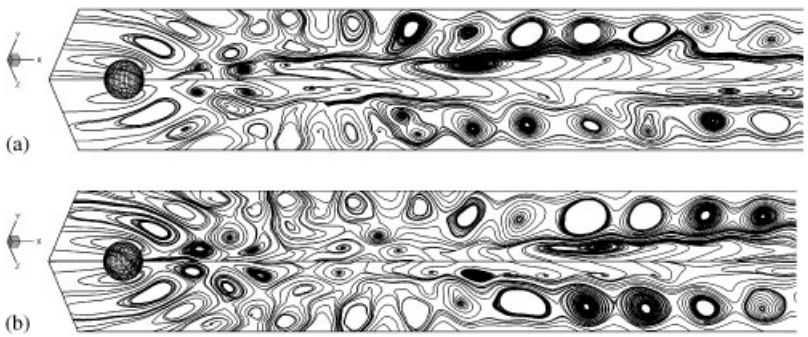

Figure 12. Instantaneous streamlines in the reference frame $\mathbf{S}_2$ at $Ro = 1$, $Re = 500$ and $B = 5$: (a) $|\mathbf{\Omega}_S| = |\mathbf{\Omega}|/2$; (b) $|\mathbf{\Omega}_S| = 0$.

4.4. Effect of the rotating angular velocity of the sphere on flow field

When a sphere moves along the axis of a rotating fluid, as that visualized experimentally [23, 24], the sphere may be driven to rotate about the axis due to the viscous force acting on the sphere. The rotating velocity of the sphere depends on some parameters in the physical problem, such as the rotating angular velocity of the cylinder, the translation velocity of the sphere, the fluid viscosity, the size and density of the sphere and so on. In the present study, the rotating angular velocity of the sphere is given in advance without solving the coupled equations of the fluid flow and the sphere motion. Yet, we need to check how the flow is affected by the rotating speed of the sphere.

To depict the effect of the rotating angular velocity ($\mathbf{\Omega}_S$) of the sphere on inertia wave cells, Figure 12 shows the streamlines in the reference frame $\mathbf{S}_1$ in two perpendicular meridian planes (i.e. $\theta = 0°$, $\pi/2$) at $Re = 500$, $B = 5$, and $|\mathbf{\Omega}_S| = |\mathbf{\Omega}|/2$ and 0, respectively. By comparing with the flow pattern in Figure 7(a) for $|\mathbf{\Omega}_S| = |\mathbf{\Omega}|$, the structures of wave cells in the outer region of the wake are almost the same for different $\mathbf{\Omega}_S$'s. The flow fields in the core wake of the sphere, however, do behave differently due to the rotating effect on the vortex shedding. It can be confirmed that the sphere rotating angular velocity $|\mathbf{\Omega}_S|$ only influences the flow picture in the central region of the wake remarkably but little on the inertia wave cells in the region out of the wake.

4.5. Evolution and formation of 'Taylor column' at small Rossby number

When the Rossby number is small enough, the dominance of Coriolis force in a rotating flow results in a flow distinctly different from the wave pattern. In this circumstance, the motion in the transverse plane is decoupled with the motion parallel to the axis of the rotation and reduces to a two-dimensional motion. According to the Taylor–Proudman theorem for the inviscid flow, a column of fluid is pushed ahead of the body that moves parallel to the rotating axis at small Rossby number, and a so-called 'Taylor column' of fluid parallel to the axis forms. At the edge of the column there exists a sharp shear layer. Naturally, it is expected that the approximation of the inviscid flow theory may be applicable to the flow at large *Re* and small *Ro*. Here, we will numerically examine that to what extent the Taylor–Proudman theorem is valid for the rotating viscous flow past a rigid body at large Reynolds numbers.

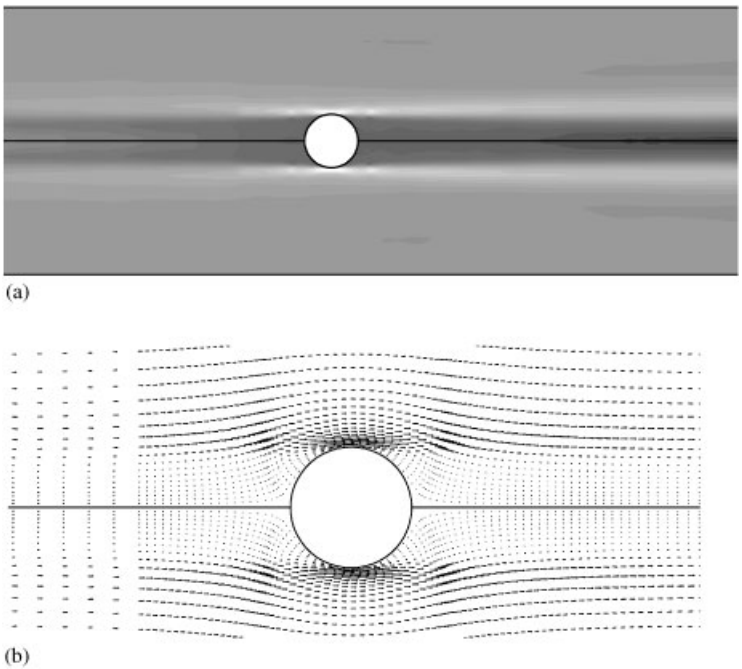

Figure 13. Flow patterns in the reference frame $\mathbf{S}_2$ in the meridian plane at $Ro = 0.02$, $Re = 500$, $B = 5$ and $|\mathbf{\Omega}_S| = |\mathbf{\Omega}|$: (a) gray picture of the axial velocity component, (b) velocity vectors.

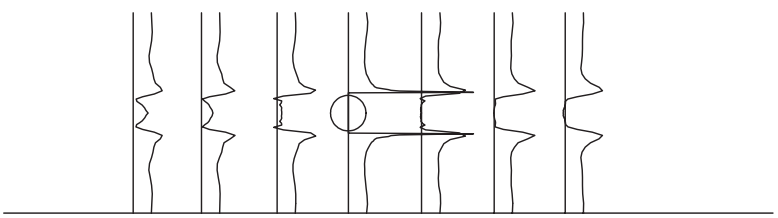

Figure 14. Profiles of the axial velocity component in the reference frame $\mathbf{S}_2$ at several different axial locations.

Figure 13 shows the flow patterns at $Ro = 0.02$, $Re = 500$, $B = 5$, and $|\mathbf{\Omega}_S| = |\mathbf{\Omega}|$. The gray picture of the axial velocity component and the velocity vector in the meridian plane are given in Figures 13(a) and 13(b), respectively. It is seen that the 'Taylor column' is indeed formed before and behind the sphere. At the edge of the 'Taylor column', the axial velocity component has a sharp change where the vorticity is very large. On the lateral sides of the sphere, high-speed stripes (white colour) appear, a character of the flow past a solid body at large Reynolds number. In addition, a thin boundary layer is presented in the proximity of the spherical surface and slightly curved streamlines are exhibited in outer regions lateral to the sphere, which deviate the prediction by the Taylor–Proudman theorem.

To illustrate the velocity variation near the edge of the 'Taylor column', Figure 14 shows the axial velocity profiles in the reference frame $\mathbf{S}_2$ at several axial locations. Toward the

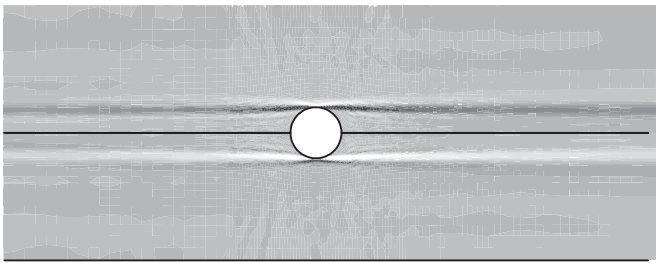

Figure 15. Gray picture of the azimuthal vorticity component in the meridian plane.

outer side of the 'Taylor column', the velocity increases quickly to form a peak and gradually changes to a uniform velocity profile with nearly the same magnitude of the incoming flow. Inside the 'Taylor column', a 'dead water' region is formed immediately behind the sphere and small but non-zero velocity is seen before the sphere. As the flow approaches the sphere, the velocity before the sphere gets smaller and smaller. From the velocity profile, it can be seen that a strong shear layer appears near the edge of the 'Taylor column'. Figure 15 shows gray picture of the azimuthal relative vorticity component in the meridian plane, which also indicates that strong vorticity is formed at the edge of the 'Taylor column'.

What is more interesting is the evolutional process of the Taylor column after the sphere starts to move. As a matter of fact, the so-called 'Taylor column' at small Ro and large Re is not immediately formed at the beginning of the sphere's movement. The time trajectory of the formation of the Taylor column is traced by using our calculated results, which is hardly observed by experiments. Figure 16 shows instantaneous streamlines in the reference frame $\mathbf{S}_2$ at several instants during the initial stage of the formation of the 'Taylor column'. One can imagine that when the sphere suddenly moves at a finite velocity U, a pressure impulse occurs immediately in response to the action of the sphere, which is very large in the near field and decays rapidly in the far field. Momentarily, the rotating fluid behaves as an inviscid flow and the viscous diffusion does not yet play a significant role. Then a cylindrical vortex sheet forms before and behind the sphere. Later, the vortex sheet oscillates and rolls up due to the Kelvin instability and to the centrifugal instability in the presence of such strong rotation. Then, for example, at $t = 0.1$, two vortex rings are formed behind and before the sphere. Because of the motion of the sphere, the vortex rings are not fore-and-aft symmetric about the sphere. As the sphere moves ahead, the vortex pair generated at the early stage gradually breaks up into smaller vortices, meanwhile, new vortex rings occur at the distant locations from the sphere. This process of evolution goes on with time, accompanying the generation of a series of vortices. As time moves on, all vortices produced in this way are dissipated, and the Taylor column consisting of nearly 'dead' flow zone is formed eventually.

5. CONCLUSIONS

Rotating viscous flows induced by a sphere moving along the axis of a rotating cylindrical container filled with the fluid are investigated by solving the three-dimensional Navier–Stokes equations using a finite element method. Numerical simulations are carried out at $Ro = 1$

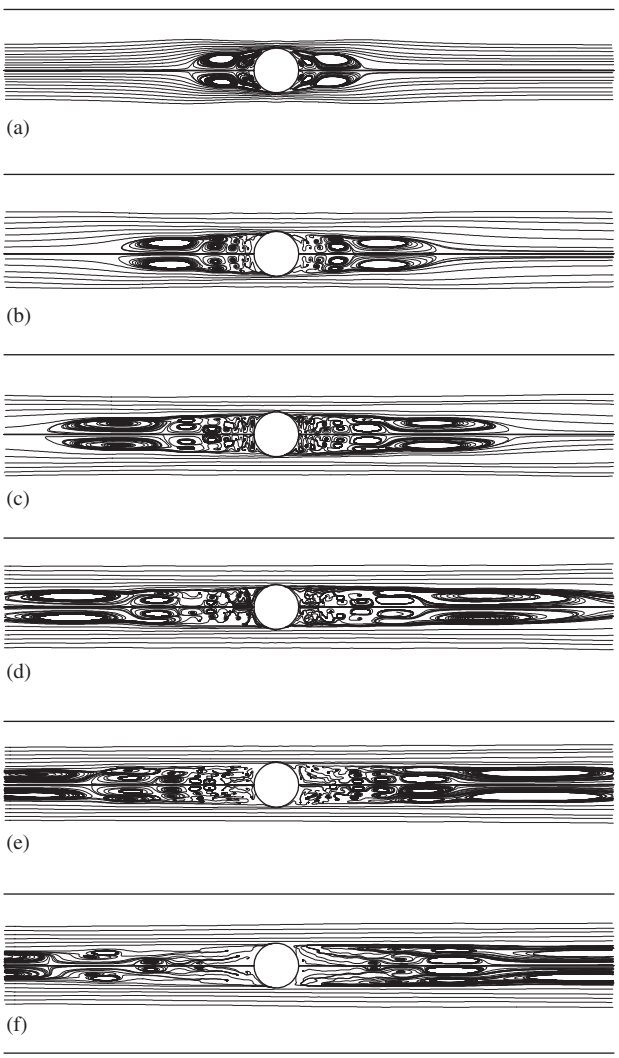

Figure 16. Instantaneous streamlines in the reference frame $\mathbf{S}_2$ at several instants during the initial stage of the formation of the 'Taylor column': (a) $t = 0.1$; (b) $t = 0.2$; (c) $t = 0.3$; (d) $t = 0.4$; (e) $t = 0.5$; (f) $t = 0.6$.

and 0.02, and $Re = 200$ and 500, respectively. Our purpose is to examine the possibility of the generation of inertia wave and its flow characters at moderate Rossby numbers (here, $Ro = 1$), and the applicability of the Taylor–Proudman theorem to viscous flow at small Rossby numbers (here, $Ro = 0.02$), in particular, the process of generation of the Taylor column. Based on this investigation, we can reach the following conclusions.

At moderate Rossby number, the inertia wave may possibly be generated for the rotating flow past a sphere at large Reynolds number. The number of the wave train increases with the increase of the ratio of the rotating cylinder radius to that of the sphere. The wave pattern

in the region out of the wake has a similar structure for different rotating angular velocities of the sphere and is almost steady relative to the frame fixed to the sphere. However, in the core region of the wake, the strong rotation of the sphere will change significantly the vortex shedding and the flow behaves unsteadily. At small Rossby number, the so-called 'Taylor column' is also found in the rotating viscous flow and strong shear layers are formed at the edges of the column where the vorticity is very large. In the initial stage of the 'Taylor column' generation, two vortex rings of different sizes are generated before and behind the sphere, respectively, and then pushed to further upstream and left to further downstream. After a dissipation course of the vortex rings during a sufficient time interval, 'dead flow' zones before and behind the sphere are formed and the 'Taylor column' appears eventually. It should be remarked that the results given in the present paper are only some typical flow pictures at a few Reynolds and Rossby numbers. The characters and mechanisms of the rotating flow past a solid body in a full range of Reynolds and Rossby numbers are still far from clearly understood and need to be investigated further by numerical analyses and experimental observations.

ACKNOWLEDGEMENTS

This work was supported by the National Science Fund for Distinguished Scholars (No. 10125210), the Innovation Project of the Chinese Academy of Sciences (No. KJCX-SW-L04), and the Programme of Hundred-Talent of the Chinese Academy of Sciences.

REFERENCES

1. Tobak M, Peake DJ. Topology of three-dimensional separated flows. *Annual Review of Fluid Mechanics* 1982; **14**:61–85.
2. Taneda S. Experimental investigation of the wake behind a sphere at low Reynolds numbers. *Journal of Physical Society of Japan* 1956; **11**:1104–1108.
3. Magarvey RH, Bishop RL. Transition ranges for three-dimensional wakes. *Canadian Journal of Physics* 1961; **39**:1418–1422.
4. Achenbach E. Vortex shedding from spheres. *Journal of Fluid Mechanics* 1974; **62**:209–221.
5. Nakamura I. Steady wake behind a sphere. *Physics of Fluids* 1976; **19**:5–8.
6. Tomboulides AG. Direct and large-eddy simulation of wake flow: flow past a sphere. *Ph.D. Thesis*, Princeton University, 1993.
7. Sakamoto H, Haniu H. The formation mechanism and shedding frequency of vortices from a sphere in uniform shear flow. *Journal of Fluid Mechanics* 1995; **287**:151–171.
8. Sakamoto H, Haniu H. A study on vortex shedding from spheres in a uniform flow. *Transactions of ASME Journal of Fluids Engineering* 1990; **112**:386–392.
9. Johnson TA, Patel VC. Flow past a sphere up to a Reynolds number of 300. *Journal of Fluid Mechanics* 1999; **378**:19–70.
10. Kim HJ, Durbin PA. Observations of the frequencies in a sphere wake and of drag increase by acoustics excitation. *Physics of Fluids* 1988; **31**:3260–3265.
11. Tomboulides AG, Orszag SA, Karniadakis GE. Direct and large-eddy simulation of axisymmetric wakes. *AIAA Paper* 93-0546, Reno, 1993.
12. Natarajan R, Acrivos A. The instability of the steady flow past sphere and disks. *Journal of Fluid Mechanics* 1993; **254**:322–344.
13. Shirayama S. Flow past a sphere: topological transitions of the vorticity field. *AIAA Journal* 1992; **30**: 349–358.
14. Rubinow SI, Keller JB. The transverse force on a spinning sphere moving in a viscous fluid. *Journal of Fluid Mechanics* 1961; **11**:447–459.
15. Barkla HM, Auchterlonie LJ. The Magnus and Robins effect on rotating spheres. *Journal of Fluid Mechanics* 1971; **47**:437–447.
16. Tsuji Y, Morikawa Y, Mizuno O. Experimental measurement of the Magnus force on a rotating sphere at low Reynolds numbers. *Transactions of ASME Journal of Fluids Engineering* 1985; **107**:484–488.

17. Oesterle B, Dinh TB. Experiments on the lift of a spinning sphere in a range of intermediate Reynolds numbers. *Experiments in Fluids* 1999; **25**:16–22.
18. Kurose R, Komori S. Drag and lift forces on a rotating sphere in a linear shear flow. *Journal of Fluid Mechanics* 1999; **384**:183–206.
19. Schlichting H. *Boundary Layer Theory* (7th edn). McGraw-Hill: New York, 1979.
20. Wang YX, Lu XY, Zhuang LX. Finite element analysis of viscous flow past a rotating sphere. *Journal of Hydrodynamics B* 2001; **13**(2):80–85.
21. Kim D, Choi H. Laminar flow past a sphere rotating in the streamwise direction. *Journal of Fluid Mechanics* 2002; **461**:365–386.
22. Batchelor GK. *An Introduction to Fluid Dynamics*. Cambridge University Press: Cambridge, 1967; 564–567.
23. Taylor GI. The motion of a sphere in a rotating liquid. *Proceedings of the Royal Society of London A* 1922; **102**:180–189.
24. Long RR. Steady motion around a symmetrical obstacle moving along the axis of a rotating liquid. *Journal of Meteorology* 1953; **10**:197–203.
25. Stewartson K. On almost rigid rotations. *Journal of Fluid Mechanics* 1957; **3**:17–26.
26. Stewartson K. On almost rigid rotations, Part 2. *Journal of Fluid Mechanics* 1966; **26**:131–144.
27. Moore DW, Saffman PG. The rise of a body through a rotating fluid in a container of finite length. *Journal of Fluid Mechanics* 1968; **31**:635–642.
28. Maxworthy T. The observed motion of a sphere through a short, rotating cylinder of fluid. *Journal of Fluid Mechanics* 1968; **31**:643–655.
29. Leibovich S. Magnetohydrodynamic flow at a rear stagnation point. *Journal of Fluid Mechanics* 1967; **29**: 401–413.
30. Buckmaster JD. Separation and magnetohydrodynamics. *Journal of Fluid Mechanics* 1969; **38**:481–498.
31. Walker JDA, Stewartson K. Separation and the Taylor-column problem for a hemisphere. *Journal of Fluid Mechanics* 1974; **66**:767–789.
32. Pritchard WG. The motion generated by a body moving along the axis of a uniformly rotating fluid. *Journal of Fluid Mechanics* 1969; **39**:443–464.
33. Maxworthy T. The flow created by a sphere moving along the axis of a rotating, slightly viscous fluid. *Journal of Fluid Mechanics* 1970; **40**:453–479.
34. Kovacs A, Kawahara M. A finite element scheme based on the velocity correction method for the solution of the time-dependent incompressible Navier–Stokes equations. *International Journal for Numerical Methods in Fluids* 1991; **13**:403–423.
35. Wang YX, Lu XY, Zhuang LX, Tang ZM, Hu WR. Numerical simulation of drop Marangoni migration under microgravity. *Acta Aeronautica* 2004; **54**:325–335.
36. Constantinescu GS, Squires KD. LES and DES investigations of turbulent flow over a sphere. *AIAA Paper* 2000-0540, Reno, 2000.
37. Fornberg B. Steady viscous flow past a sphere at high Reynolds numbers. *Journal of Fluid Mechanics* 1988; **190**:471–489.
38. Magnaudet J, Rivero M, Fabre J. Accelerated flows past a rigid sphere or a spherical bubble, Part 1. Steady straining flow. *Journal of Fluid Mechanics* 1995; **284**:97–135.
39. Pruppacher HR, Le Clair BP, Hamielec AE. Some relations between drag and flow pattern of viscous flow past a sphere and a cylinder at low and intermediate Reynolds numbers. *Journal of Fluid Mechanics* 1970; **44**:781–790.

